

Reconstruction of the Apollo 11 Moon Landing Final Descent Trajectory

*Luke J. Miller, Jared A. Grauer, and Jing Pei
Langley Research Center, Hampton, Virginia*

*Stewart L. Nelson
Advanced Aircraft Company, Hampton, Virginia*

National Aeronautics and
Space Administration

Langley Research Center
Hampton, Virginia 23681-2199

August 2022

The use of trademarks or names of manufacturers in this report is for accurate reporting and does not constitute an official endorsement, either expressed or implied, of such products or manufacturers by the National Aeronautics and Space Administration.

Available from:

NASA STI Program / Mail Stop 148
NASA Langley Research Center
Hampton, VA 23681-2199
Fax: 757-864-6500

Abstract

Relatively limited data on the Apollo 11 pre-planned and as-flown trajectories are available in the open literature and in the NASA archives. Furthermore, a single report appears to be the only source containing plots comparing the pre-planned and as-flown final approach and landing trajectories. The plots in that report, however, are small and difficult to read, and contain data that are insufficient for directly reconstructing the final landing trajectory. In this report, several published graphics are digitized, and then a variety of least-squares and Kalman filter estimators are applied using kinematic equations and simplified dynamic equations to reconstruct the final descent trajectory. The reconstructed trajectory is important in the crew training effort for program Artemis, which intends to send humans back to the moon, as well as other studies focusing on landing on extraterrestrial worlds.

Contents

| | |
|---|----|
| Nomenclature | 3 |
| 1 Introduction | 5 |
| 2 Landing Phase Description | 6 |
| 3 Digitization of Data | 6 |
| 4 Altitude / Altitude-Rate Profile Reconstruction | 7 |
| 5 Range Trajectory Reconstruction | 9 |
| 6 Total Trajectory | 10 |
| 7 Conclusions | 11 |
| 8 Acknowledgements | 11 |
| References | 12 |
| Appendix A – The Kalman Filter | 13 |
| Appendix B – Planar Dynamics Model of the Lander | 15 |
| Figures | 16 |

Nomenclature

Roman

| | |
|---------------|---|
| A | state matrix |
| B | control input matrix |
| C | output matrix |
| D | feedthrough matrix |
| ∂ | partial derivative |
| \mathbb{E} | expectation operator |
| g | acceleration due to gravity near the lunar surface, = 5.315 ft/s ² |
| h | altitude above lunar surface, ft |
| \mathbb{I} | identity matrix |
| K | Kalman gain matrix |
| M | information matrix |
| m | spacecraft mass, slug |
| N | number of data samples |
| \mathcal{N} | normal distribution |
| P | state vector error covariance matrix |
| Q | process noise covariance matrix |
| q | body-axis pitch rate, rad/s |
| R | measurement noise covariance matrix |
| R^2 | coefficient of determination |
| S | innovation covariance matrix |
| T | thrust magnitude, lbf |
| t | time, s |
| u | input |
| v | modeling residuals vector |
| w | process noise input |
| x | state vector |
| x | range position to landing site, ft |
| y | output |

Greek

| | |
|------------|--|
| Γ | discrete-time control input matrix |
| Δt | sample period, s |
| θ | unknown parameters |
| θ | pitch angle, rad |
| Λ | discrete-time process noise input matrix |
| ν | modeling innovations vector |
| Φ | state transition matrix |

Superscripts

| | |
|---------------------|-----------------|
| \cdot | time derivative |
| $\hat{}$ | estimated value |
| $^{-1}$ | inverse |
| T | transpose |

Acronyms

| | |
|-----|----------------------------|
| CSM | Command and Service Module |
|-----|----------------------------|

| | |
|-----|----------------------------|
| DOI | Descent Orbit Insertion |
| HLS | Human Landing System |
| LGC | LM Guidance Computer |
| LM | Lunar Module |
| PDI | Powered Descent Initiation |

1 Introduction

Currently, the Human Landing System (HLS), which is part of the NASA Artemis Program [1], seeks to land the first woman and the next man on the lunar surface with a target destination of the lunar south pole in the year 2025. The final descent and landing phases of the mission are expected to be critical to the overall mission success but also involve the greatest amount of risk to the onboard crew and the lunar lander. As a result, the design of the final descent and landing phase of the mission is prioritized.

So far, there have been only six successful crewed missions that have landed on the moon: Apollo 11, 12, and 14–17. These six missions represent the only sources of information for future crewed missions. The data recorded from these missions is useful for learning from past experiences, designing and optimizing future mission trajectories, developing ground-based and in-flight training platforms for astronauts, and other applications.

The trajectory data from Apollo 11, which was the first mission to successfully land crew on the lunar surface, are of particular importance. During landing phase, the Lunar Guidance Computer (LGC) program P-64 provided automated guidance commands to fly the Lunar Module (LM), illustrated in Fig. 1, towards designated landing targets. Near the landing site, program P-65 was to then automatically null the translational velocities before performing a vertical descent. However, during Apollo 11, the LM was headed towards rough terrain near the West Crater because of various navigation errors and Commander Armstrong took manual control of the spacecraft, initiating program P-66, and flew the LM approximately 1,100 ft down range of the original target to its historic landing.

Despite these deviations from the nominal trajectory, the Apollo 11 landing represents a precious record in the short list of crewed moon landings. Unfortunately, most of the original magnetic data tapes from the Apollo missions have been erased and reused [2,3] or otherwise lost to time. Only a small amount of data on the Apollo 11 trajectories remain, including publications and other documentation made at the time. The conference paper and technical memorandum by Bennett [4] appears to be the only document that contains plots of both the planned (automatically targeted by the guidance computer) and actual (flown) trajectories of Apollo 11 in the longitudinal plane. However, these plots are of relatively poor resolution, contain possible errors, and provide incomplete information for reproducing the trajectory time histories needed for further analysis and utility. Other documents, such as Ref. [5], provide other pieces of data but are not entirely consistent with those in other documents such as Ref. [4]. In an attempt to reconstruct trajectories from Apollo missions, some works have sought to construct complicated dynamics of the spacecraft and solve the equations of motion using measured time histories of the pilot inputs [6–8].

In this work, the actual trajectories from the Apollo 11 descent and landing are similarly sought. Instead of constructing dynamic models to solve the equations of motion based on measured pilot input time histories, data provided as plots in Ref. [4] were digitized and analyzed. Kinematic and simplified dynamic relationships are combined with state estimators and digitized data to reconstruct the data. The end result is a synchronized collection of time histories for the Apollo 11 planar range, altitude, and pitch angle, as well as the first and second derivatives of those variables. This approach has the benefit that it is rooted in the published literature and does not require the construction of a complicated and high-fidelity model of the Lunar Module system.

The remainder of the report is organized as follows. Section 2 summarizes the Apollo 11 landing phase of the trajectory. Section 3 describes the digitization of the plots given in Ref. [4]. Section 4 details the approach for reconstructing the altitude and altitude rate time histories. Similarly, Section 5 details the approach applied to reconstructing the range position and forward velocity time histories. Section 6 summarizes the total reconstruction of the final descent trajectory. Section 7 provides further discussion and concludes the report.

2 Landing Phase Description

Upon nearing the moon, the joined LM and Command and Service Module (CSM) entered into a parking orbit between 58 and 62 nautical miles in altitude. The LM undocked from the CSM, separated by several hundred feet, and then performed a descent orbit insertion (DOI) to reduce its altitude to about 50,000 ft.

Afterwards, a powered descent initiation (PDI) was performed to land on the lunar surface. The PDI consisted of three parts: the braking phase, the approach phase, and the final (or landing) phase. The braking phase was to reduce the orbital velocity, resulting in the “high gate” conditions. The approach phase is for the pilot to monitor the approach and ends in the “low gate” conditions. The landing phase facilitated continued monitoring of the lander trajectory by the pilots, and had the option of manual control during the final touchdown. Figure 2, taken from Ref. [4], shows an illustration of this trajectory.

This report concerns only the final landing phase of the Apollo 11 moon landing. More details on the descent trajectory are given in Refs. [4, 5, 9–13] and others.

3 Digitization of Data

The original data recorded from the Apollo 11 moon landing are no longer available. Consequently, data for reconstructing the trajectory were obtained by digitizing plots from published works, primarily Ref. [4]. This section summarizes that process.

Three plots providing information on the final landing phase trajectory were digitized. These three original plots, taken from Ref. [4], are shown in Fig. 3. The first plot, Fig. 3a, is the range profile to landing site shown as altitude vs. range. The actual landing took place about 1,100 ft down range of the planned landing site. The second plot, Fig. 3b, is the attitude profile, shown as the inertial pitch angle vs. time. According to the body-axis conventions shown in Fig. 1 and description in Ref. [14], the pitch angle is the pilot centric and given as the rotation about the Y_B axis from the nominal upright attitude. The third plot, Fig. 3c, is the altitude / altitude-rate profile, shown as altitude vs. the descent velocity.

These images were digitized using GRABIT [15], which is a freely-available graphical program written in MATLAB®. Figure 4 shows a screenshot of this process using the altitude / altitude-rate profile from Fig. 3c. After loading an image of a plot, pixels were selected that corresponded to the ends of the horizontal and vertical axes. These are shown as the larger red and blue circles with crosshairs. Based on this information, the program calibrates the conversion from pixels in the image to physical engineering units. After this initial process, data were digitized by clicking pixels along the plotted trajectory. These points are the smaller red dots in Fig. 4. A small preview is also displayed in the upper right corner of the display. The recorded data are then saved as a `.mat` file native to MATLAB®.

The number of samples to digitize represents a tradeoff between resolution on the plot and amount of computation time needed to process the data using the approaches discussed in the following sections. Several attempts were made at digitizing the data, and the final results had 113 samples for Figure 3a, 138 samples for Fig. 3b, and 194 samples for Fig. 3c. These numbers represented a satisfactory subjective tradeoff. An effort was made to increase the density of samples at points where the data had large amounts of curvature. In digitizing Fig. 3c, an effort was also made to increase the sampling density for lower altitude rates, which had the effect of keeping the samples evenly distributed over time.

The digitization was performed carefully because errors inadvertently introduced during this process impacts the final reconstructed trajectory. However, some errors were inevitable. The original plots, particularly the range profile in Fig. 3a, were small on the page, blurry, and had poor spatial resolution.

In addition to digitization errors, there are also errors apparent in the data itself. Some of these errors could have come from time skews, measurement noise, sensor errors, the original processing of the data, neglected lateral dynamics, or other factors. To provide a sense of the extent to which errors may be present, consider Fig. 5. The blue line is the digitized altitude / altitude-rate profile from Ref. [4]. The red line

was formed from data in the Apollo 11 Guidance, Navigation, and Control Systems Performance Analysis Report [5]. The altitude rate time history was digitized from Fig. 6.14 in Ref. [5] and then numerically integrated to form the trajectory shown. Note the bias in altitude, higher frequency content, and different shape to the profile throughout the landing maneuver.

Another concern with the altitude / altitude-rate profile data from Ref. [4] was the presence of kinematic errors. When the altitude rate is negative (left half side of Fig. 3c), the altitude should be decreasing, and vice versa, by definition. However, there are a few sections of Fig. 3c where this does not hold. For example, just below 160 ft altitude, the altitude rate is negative but the altitude begins to decrease. An effort was made to attempt to account for possible errors in the landing radar antenna axes described in Ref. [4], but did not improve the results. Rather, kinematically inconsistent points were identified and replaced with interpolated values. This applied to three points near 160 ft, and to two points near 10 ft.

4 Altitude / Altitude-Rate Profile Reconstruction

This section describes the process in which the digitized data from Fig. 3c was processed to obtain time histories of the altitude and altitude rate from the altitude / altitude-rate profile. The vector of time samples in this plot is implicit and not directly evident. This is in contrast to time histories, for example Fig. 3b, in which time is explicit. Therefore, more information is needed to determine the time samples for the digitized data of the trajectory.

The horizontal and vertical axes of Fig. 3c are related through a derivative. This relationship can be written as the kinematic equation

$$h(t) = h(0) + \int_0^t \dot{h}(\tau) d\tau \quad (1)$$

where $h(t)$ is the altitude, $\dot{h}(t)$ is the altitude rate or descent velocity, and $h(0)$ is the altitude when P-66 was initiated (corresponding to the mission time of 102 hours, 43 minutes, and 20 seconds).

A nonlinear optimization was performed using the MATLAB[®] function `fmincon.m` to estimate values in the time vector (time stamps) that corresponded to the data digitized from Fig. 3c. Initially, the digitized altitude-rate data were used as inputs to integrate Eq. (1) using a trapezoidal method from a given set of time estimates. Reference [4] indicated the initial altitude was $h(0) = 410$ ft and the initial descent rate was $\dot{h}(0) = -10$ ft/s. Starting values for the time vector are discussed next. Based on the integrated result for the altitude, a least-squares cost function

$$J(\boldsymbol{\theta}) = \frac{1}{2} \sum_{k=1}^N v_k^2 \quad (2)$$

was minimized for the unknown time stamps, arranged in the vector $\boldsymbol{\theta}$, where

$$v_k = h_k - \hat{h}_k \quad (3)$$

is the residual error between the digitized measurement of altitude h_k and the estimate based on Eq. (1) of altitude \hat{h}_k for samples $k = 1, 2, \dots, N$. Equality constraints were included to enforce the initial time was $t = 0$ s and the final time was $t = 140$ s [4]. Inequality constraints were also included to enforce that subsequent time steps were monotonically increasing.

Starting values for the unknown time samples were initiated to be constant over the maneuver. For the 194 samples used here, this produced an average time sample period of $\Delta t = 0.715$ s.

A second approach for obtaining starting values for the time stamps was also attempted. Here the kinematic relationship from Eq. (1) was expressed in differential form, rather than integral form, as

$$\dot{h}_k = \frac{h_{k+1} - h_k}{t_{k+1} - t_k} \quad (4)$$

The unknown subsequent time step (starting from $t = 0$) was then iteratively solved for from $i = 1, 2, \dots, N$ as

$$t_{k+1} = t_k + \frac{h_{k+1} - h_k}{\dot{h}_k} \quad (5)$$

This approach for obtaining the starting values for the time stamps produced solutions very close to the final optimized values and lowered the number of iterations needed over starting the time steps at evenly distributed samples over the maneuver length. However, both sets of initial conditions converged to the same set of optimized time sample estimates. However, in subsequent processing discussed below involving a Kalman filter, this approach proved more complicated and less accurate and was abandoned.

Using trapezoidal integration to solve Eq. (1) within the optimization process produced excellent results for most of the trajectory. The optimization used 149 iterations, which took approximately 2.4 s on a standard laptop computer. However, for the last part of the landing and below about 20 ft, the match was poor. In addition, 17 samples had an approximately zero time step (set to the tolerance to which the constraints are enforced) from the previous sample, resulting in almost instantaneous changes in the altitude rate at a constant altitude. Furthermore, the predicted trajectory ended while the altitude was approximately 5 ft rather than 0 ft.

To improve the estimation results, a Kalman filter was used to solve Eq. (1) within the optimization iterations instead of using integration. The general Kalman filter equations are given in detail in Appendix A. This approach had the benefit of trading confidence in the model equations with confidence in the data, which was known to contain errors as previously discussed.

The Kalman filter state and output equations in Eq. (16) corresponding to Eq. (1) in discrete time were

$$x_{k+1} = x_k + \Delta t_k u_k + \Delta t_k w_k \quad (6a)$$

$$y_k = x_k \quad (6b)$$

where the state and output are the predicted altitude and the input is the digitized altitude-rate data. The altitude rate is assumed to contain noise and error, which is why the time sample duration Δt_k in Eq. (6a) multiplies both the deterministic input and the process noise input. Note that Eq. (6) is in discrete time. Because the unknown time steps change for each data sample, Δt_k is not constant and the time-varying form of the Kalman filter was needed.

The optimization was rerun using the Kalman filter in place of trapezoidal method of integration. The MATLAB[®] function `fmincon.m` was again used with both the equality and inequality constraints. Starting values for the time stamps were selected as equidistant spacings through the maneuver. The cost function for the optimization problem to minimize was

$$J(\theta) = \frac{1}{2} \sum_{k=1}^N \left[\frac{\nu_k^2}{S_k} \right] + \frac{N}{2} \log |S_k| \quad (7)$$

where ν_k are the innovations and S_k is the innovation covariance matrix, as discussed in Appendix A. The cost function in Eq. (7) is the negative logarithm of the likelihood function used for maximum likelihood estimators considering both measurement noise and process noise [16, 17]. The cost function minimizes two terms: one that is a weighted sum of squares of the innovations, and one that reflects the size of the innovation covariance matrix.

The covariance matrices in the Kalman filter were first set according to the thickness of the lines used to draw the trajectory in Fig. 3c. Based on estimation results and the previous discussion on errors in the published data, this approach was abandoned. Instead, the covariance matrices were tuned to $Q = 4$, $R = 5$, and $P_0 = 1$. These values are not optimal, and there is some sensitivity to the results based on their values. This optimization process used 179 iterations and about 50 minutes of computation time on a standard laptop computer.

Figure 6 shows the digitized altitude / altitude rate data from Ref. [4] and the final fit to that data. The fit had a coefficient of determination R^2 of approximately 1.0, and had a root mean squared error of 0.534 ft. There was a small amount of mismatch near an altitude of 20 ft, but these results did not have the same problems with the time step going to zero that the integration method had.

Figure 7 displays the estimated time samples as blue dots. The time samples are monotonically increasing, and do not reach any constraints. There is a strong linear trend to the data, which reflects the care taken during digitization of the data in Fig. 3c. Values for the steps ranged between 0.1341 and 2.2038 s. The error bounds on the markers in Fig. 7 reflect the 95% confidence interval for these estimates. These were obtained by first numerically computing the information matrix

$$\mathbf{M} = -\mathbb{E} \left[\frac{\partial^2 J}{\partial \boldsymbol{\theta} \partial \boldsymbol{\theta}^T} \right] \quad (8)$$

as the cost function Hessian matrix after the optimization completed. Afterwards, the standard errors are the square root of the diagonal elements of the inverse of this matrix. The error bounds are reflective of the uncertainty but are not statistically accurate due to the tuning process used to choose Q , R , and P_0 .

Figure 8 shows the time histories for altitude and altitude rate, based on the digitized data from Fig. 3c and the estimated time vector. These data are synchronized together and kinematic dependencies between the altitude and altitude rate are consistent. The acceleration of altitude, used later, was obtained by numerically differentiating the synchronized altitude-rate data using a smoothing method [16,18].

5 Range Trajectory Reconstruction

Figure 3a shows the range position along the surface of the moon against the altitude. As before in Section 4, time is a parameter of the graph and not explicitly given. Therefore, time histories of altitude and range are not known directly. However, the altitude time history is known from the altitude / altitude-rate profile reconstruction discussed in Section 4. The following task was therefore to determine the time samples for the 113 digitized points from Fig. 3a that synchronized the resulting time histories to those obtained in Section 4.

This synchronization was done by estimating the time samples that best matched the altitude history from Fig. 3a to the synchronized altitude time history from Section 4 in a least-squares sense. The cost function that was optimized was

$$J(\boldsymbol{\theta}) = \frac{1}{2} \sum_{i=1}^N v_k^2 \quad (9)$$

The residuals here were defined as

$$v(i) = [t_k]_{f25} - [t_k]_{f22} \quad (10)$$

where $[t_k]_{f25}$ is the k th time sample from the synchronized data from Fig. 3c and $[t_k]_{f22}$ corresponds to the estimated time sample from Fig. 3a. Because a different number of samples were used for each of these time vectors, and because the time samples were in general not equal, the time samples from the synchronized data in Section 4 were linearly interpolated to the same altitude as the digitized data from Fig. 3a.

Figure 9 shows the optimization results. The blue line and markers show the altitude time history obtained from Section 4. The red line and markers show the initial estimate of the altitude time history from the digitized data of Fig. 3a using an equidistant time vector from 0 s to 138 s using 113 points. This initial estimate had a cost function per Eq. (9) of 25,784 and did not match well. The MATLAB® function `fmincon.m` used 11 iterations and 0.2 s of computation time to optimize the time sample estimates. These had a final cost of 2 and are shown as an orange line and markers.

The estimated time instances to synchronize the altitude time history in Fig. 3a are shown in Fig. 10. The mean standard error was about 1.0 s. These estimates have smaller uncertainty bounds than in Fig. 7 because the process and measurement covariance matrices were not needed here. The trend is approximately linear until the end of the landing, where the change between time samples increases due to the arrest of the vehicle motion at landing. The differences between time steps ranged from approximately 0 s to 12.7 s. Smallest time steps were a result of the constraints that the time vector had to be monotonically increasing, and were due to the difficulty in accuracy digitizing the data in Fig. 3a. The largest time step, 12.7 s, was for the final data point where the vehicle landed.

Synchronized data for the altitude and range time histories are shown in Fig. 11. A few high-frequency jumps are seen in the altitude data, and there are some kinks in the range data. Again, these were due to the difficulty in digitizing data from Fig. 3a. However, the general trend of the trajectories seemed plausible.

To further refine the synchronized altitude and range data from Fig. 11 and to determine derivatives of those data, the time histories were again processed using a Kalman filter. As discussed in Appendix B, the range acceleration of the longitudinal spacecraft dynamics can be related to the altitude acceleration and the pitch rate as

$$\ddot{x} = -(\ddot{h} + g) \tan \theta \quad (11)$$

This equation is a double integrator and was discretized as

$$\begin{bmatrix} x_{1_{k+1}} \\ x_{2_{k+1}} \end{bmatrix} = \begin{bmatrix} 1 & \Delta t_k \\ 0 & 1 \end{bmatrix} \begin{bmatrix} x_{1_k} \\ x_{2_k} \end{bmatrix} + \begin{bmatrix} \Delta t_k/2 \\ \Delta t_k \end{bmatrix} u_k \quad (12a)$$

$$y_k = \begin{bmatrix} 1 & 0 \end{bmatrix} \begin{bmatrix} x_{1_k} \\ x_{2_k} \end{bmatrix} + [0] u_k \quad (12b)$$

for use in a Kalman filter. The states are the range and range-rate. A time-varying Kalman filter was again used because the time steps vary throughout the data. This Kalman filter estimates the range and range-rate states that best match range data based on the measured inputs.

The input for the Kalman filter equations of motion in Eq. (12) corresponds to the entire right side of Eq. (11). The altitude acceleration was obtained from differentiating the altitude rate data from Section 4. The pitch angle data was obtained from digitizing Fig. 3b and interpolating it to the time steps used in Section 4. The digitized pitch angle time history is shown in Fig. 12.

The final reconstructions of the range data are shown in Fig. 13. From tuning, the covariance matrices were selected as $\mathbf{Q} = 0.001$, $\mathbf{R} = 1$, and $\mathbf{P}_0 = 1$. These values were based on visual inspection of the results which produced a smooth trajectory that generally followed the synchronized data but smoothed some of the high-frequency errors from digitization. The output had an R^2 value of approximately 1.0 and a root mean square error of 32.1 ft.

6 Total Trajectory

The total reconstructed trajectory of the Apollo 11 final descent to the moon is given in Fig. 14. The range, range rate, and range acceleration are given by the first column of plots. The altitude, altitude rate, and altitude acceleration are given in the second column of plots. The inertial pitch angle, body-axis pitch rate, and pitch acceleration are given by the third column of plots. All data shown were interpolated to a common time vector having a constant time step of 0.2 s or a rate of 5 Hz. This data was saved as a `.mat` file native to MATLAB[®].

Time histories for the range $x(t)$ and the range rate $\dot{x}(t)$ are provided by the Kalman filter output, as discussed in Section 5. The range acceleration $\ddot{x}(t)$ is computed using the altitude acceleration data from Section 4, the digitized pitch rate from Fig. 3b, and the equations of motion derived in Appendix B.

Time histories for the altitude and altitude rate come from the analysis in Section 4. The altitude acceleration comes from smoothly differentiating the altitude rate [16, 18].

The inertial pitch angle $\theta(t)$ comes from digitizing Fig. 3b. The body-axis pitch rate comes from smoothly differentiating the pitch angle and assuming small perturbations about longitudinal motion such that $q(t) \simeq \dot{\theta}(t)$. The pitch acceleration $\dot{q}(t)$ comes from smoothly differentiating the pitch rate.

The benefit of the approaches used in this report are that they are based upon only the digitized data and simplified kinematic or dynamic equations of motions. A detailed dynamic model of the Apollo lunar lander was not needed. Furthermore, the use of a kinematic model with a Kalman filter throughout the analysis resulted in a kinematically-consistent reconstruction of the trajectory with some states estimated that would have otherwise not been available (e.g., the range rate $\dot{x}(t)$). The disadvantages of the approaches include

the limitations and inaccuracies due to data digitization, the fact that temporal data were only implicitly given in some of the plots used, and that the Kalman filters were manually tuned by analyst judgement.

7 Conclusions

This report describes an effort to reconstruct the final descent and landing of the Apollo 11 moon landing from published data. This analysis is important for planning future manned missions to the moon, such as in the NASA Artemis program, because the original data are no longer available and there have been only six successful crewed landings.

The analysis was based on three plots from a NASA technical memorandum, published relatively soon after the Apollo 11 landing. These plots were digitized and analyzed using a variety of least-squares and Kalman filter estimators, kinematic equations, and simplified planar equations of motion. The main contribution of the paper was a complete time history of the range, altitude, and pitch trajectory, as well as the first two derivatives of those data (e.g., pitch rate and pitch acceleration).

Because the analysis was based on data and simplified relationships, the construction of a detailed simulation of the lunar lander, relating pilot inputs to response of the spacecraft, was unnecessary. Additionally, because a Kalman filter was used, the reconstructions were kinematically consistent and included some information that otherwise would not have been reconstructed.

8 Acknowledgements

This research was supported by NASA under the Human Landing System (HLS) ground-based simulation task for the Artemis program. Technical discussions with Randall Bailey and Edward Robertson are acknowledged and appreciated.

References

1. Anon.: “Artemis Plan: NASA’s Lunar Exploration Program Overview”. www.nasa.gov/sites/default/files/atoms/files/artemis_plan-20200921.pdf, September 2020.
2. Greenfieldboyce, N.: “Houston, We Erased The Apollo 11 Tapes”. National Public Radio, www.npr.org/2009/07/16/106637066/houston-we-erased-the-apollo-11-tapes, July 2009.
3. Dunbar, B.: “Not-Unsolved Mysteries: The ‘Lost’ Apollo 11 Tapes”. NASA, www.nasa.gov/feature/not-unsolved-mysteries-the-lost-apollo-11-tapes, July 2019.
4. Bennett, F.: “Apollo Lunar Descent and Ascent Trajectories”. NASA TM X-58040, March 1970.
5. Anon.: “Apollo XI Guidance, Navigation and Control Systems Performance Analysis Report”. NASA CR-108395, December 1969.
6. Lee, A.: “Fuel-Efficient Descent and Landing Guidance Logic for a Safe Lunar Touchdown”. *Guidance, Navigation, and Control Conference*, AIAA Paper 2011-6499, August 2011.
7. Sagliano, M.: “Apollo 11 Reloaded: Optimization-Based Trajectory Reconstruction”. *Guidance, Navigation, and Control Conference*, AIAA Paper 2021-1344, January 2021.
8. Olsen, J.; and Bettinger, R.: “Six Degree-of-Freedom Analysis of the Apollo 10 Atmospheric Reentry”. *SciTech Forum*, AIAA Paper 2022-2273, January 2022.
9. Bennett, F.; and Price, T.: “Study of Powered-Descent Trajectories for Manned Lunar Landings”. NASA TN D-2426, August 1964.
10. Cheatham, D.; and Bennett, F.: “Apollo Lunar Module Landing Strategy”. NASA TM X-58006, July 1966.
11. Ertel, I.; and Morse, M.: “The Apollo Spacecraft. Volume I: A Chronology”. NASA SP-4009, January 1969.
12. Anon.: “Apollo 11 Mission Report”. NASA SP-238, January 1971.
13. Bennett, F.: “Apollo Experience Report — Mission Planning for Lunar Module Descent and Ascent”. NASA TN D-6846, June 1972.
14. Stengel, R.: “Manual Attitude Control of the Lunar Module”. *Journal of Spacecraft and Rockets*, vol. 7, no. 8, August 1970, pp. 941–948.
15. Jiro: GRABIT. <https://www.mathworks.com/matlabcentral/fileexchange/7173-grabit>, accessed January 2022.
16. Morelli, E.; and Klein, V.: *Aircraft System Identification: Theory and Practice*. Sunflyte Enterprises, 2016.
17. Grauer, J.; and Morelli, E.: “A New Formulation of the Filter-Error Method for Aerodynamic Parameter Estimation in Turbulence”. *Atmospheric Flight Mechanics Conference*, AIAA Paper 2015-2704, June 2015.
18. Morelli, E.: System IDentification Programs for AirCRAFT (SIDPAC). version 4.1, NASA Software Catalog, <https://software.nasa.gov/software/LAR-16100-1>, accessed February 2022.
19. Gelb, A.; et al.: *Applied Optimal Control*. The M.I.T. Press, 1974.
20. Simon, D.: *Optimal State Estimation*. John Wiley & Sons, Inc., 1974.

A – The Kalman Filter

This section develops the Kalman filter equations used in this report. For more details on the Kalman filter and its implementation, see Refs. [16, 19, 20].

Consider the linear time-invariant (LTI) system in continuous time

$$\dot{\mathbf{x}}(t) = \mathbf{A} \mathbf{x}(t) + \mathbf{B} \mathbf{u}'(t) \quad (13)$$

where $\mathbf{x}(t)$ is the state and $\mathbf{u}'(t)$ is the measured input. When the measured input contains measurement noise, it can be decomposed as

$$\mathbf{u}'(t) = \mathbf{u}(t) + \mathbf{w}(t) \quad (14)$$

where $\mathbf{u}(t)$ is the actual input and $\mathbf{w}(t)$ is the measurement noise. Substituting Eq. (14) into (13) results in the canonical state-space model for an LTI system with process noise

$$\dot{\mathbf{x}}(t) = \mathbf{A} \mathbf{x}(t) + \mathbf{B} \mathbf{u}(t) + \mathbf{B} \mathbf{w}(t) \quad (15a)$$

Similarly, the output equations are

$$\mathbf{y}(t) = \mathbf{C} \mathbf{x}(t) + \mathbf{D} \mathbf{u}(t) + \mathbf{D} \mathbf{w}(t) \quad (15b)$$

The continuous-time model in Eq. (15) can be transformed into the discrete-time model at samples k as

$$\mathbf{x}_{k+1} = \mathbf{\Phi}_k \mathbf{x}_k + \mathbf{\Gamma}_k \mathbf{u}_k + \mathbf{\Gamma}_k \mathbf{w}_k \quad (16a)$$

$$\mathbf{y}_k = \mathbf{C}_k \mathbf{x}_k + \mathbf{D}_k \mathbf{u}_k + \mathbf{D}_k \mathbf{w}_k \quad (16b)$$

with measurements of the outputs

$$\mathbf{z}_k = \mathbf{y}_k + \mathbf{v}_k \quad (16c)$$

where \mathbf{v}_k is the measurement noise. The matrices in Eq. (16a) are defined as

$$\mathbf{\Phi}_k = e^{\mathbf{A}\Delta t_k} \quad (17a)$$

$$\mathbf{\Gamma}_k = \left(\int_0^{\Delta t_k} e^{\mathbf{A}\tau} d\tau \right) \mathbf{B} \quad (17b)$$

This discretization assumes a zero-order hold sampling on the input using the sample periods Δt_k . Although the continuous-time model in Eq. (15) is LTI, the system matrices for the discrete-time model in Eq. (16) are linear time-varying (LTV) because a variable sampling rate is used in this work. The process noise (measurement noise on the inputs) and measurement noise on the outputs are assumed to be Gaussian white processes with

$$\mathbf{w}_k \sim \mathcal{N}(\mathbf{0}, \mathbf{Q}_k) \quad (18a)$$

$$\mathbf{v}_k \sim \mathcal{N}(\mathbf{0}, \mathbf{R}_k) \quad (18b)$$

The discrete-time, time-varying Kalman filter is initiated using an estimate of the initial conditions

$$\hat{\mathbf{x}}_0 \sim \mathcal{N}(\mathbf{x}(t_0), \mathbf{P}_{0|0}) \quad (19)$$

The predicted (a priori) state estimate and state error covariance are

$$\hat{\mathbf{x}}_{k|k-1} = \mathbf{\Phi}_{k-1} \hat{\mathbf{x}}_{k-1|k-1} + \mathbf{\Gamma}_{k-1} \mathbf{u}_{k-1} \quad (20a)$$

$$\mathbf{P}_{k|k-1} = \mathbf{\Phi}_{k-1} \mathbf{P}_{k-1|k-1} \mathbf{\Phi}_{k-1}^T + \mathbf{\Gamma}_{k-1} \mathbf{Q}_{k-1} \mathbf{\Gamma}_{k-1}^T \quad (20b)$$

The measurement update begins with computing the innovation (measurement pre-fit difference) and the innovation covariance

$$\boldsymbol{\nu}_k = \mathbf{z}_k - \mathbf{C}_k \hat{\mathbf{x}}_{k|k-1} - \mathbf{D}_k \mathbf{u}_k \quad (21a)$$

$$\mathbf{S}_k = \mathbf{C}_k \mathbf{P}_{k|k-1} \mathbf{C}_k^T + \mathbf{R}_k \quad (21b)$$

The optimal Kalman gain is then computed as

$$\mathbf{K}_k = \mathbf{P}_{k|k-1} \mathbf{C}_k^T \mathbf{S}_k^{-1} \quad (22)$$

The updated (a posteriori) state estimate and state error covariance are

$$\hat{\mathbf{x}}_{k|k} = \hat{\mathbf{x}}_{k|k-1} + \mathbf{K}_k \boldsymbol{\nu}_k \quad (23a)$$

$$\mathbf{P}_{k|k} = (\mathbb{I} - \mathbf{K}_k \mathbf{C}_k) \mathbf{P}_{k|k-1} (\mathbb{I} - \mathbf{K}_k \mathbf{C}_k)^T + \mathbf{K}_k \mathbf{R}_k \mathbf{K}_k^T \quad (23b)$$

The associated output estimate, based on the updated state estimate, is

$$\hat{\mathbf{y}}_k = \mathbf{C}_k \hat{\mathbf{x}}_{k|k} + \mathbf{D}_k \mathbf{u}_k \quad (24)$$

B – Planar Dynamics Model of the Lander

This appendix derives the equations of motion used for the estimation procedure discussed in Section 5. To start, consider the simplified planar model of a rigid-body spacecraft landing on the moon surface, as shown in Fig. 15. An inertial frame is assumed on the surface of the moon with the a unit vector pointing in the range direction \mathbf{n}_1 and a unit vector in the downward direction \mathbf{n}_3 . The lander also has a body-fixed frame at the instantaneous center of mass with the x -axis unit vector \mathbf{b}_1 pointing up and the z -axis unit vector \mathbf{b}_3 pointing out the pilot window, as in Fig. 1 and Refs. [4, 14].

With respect to the inertial frame, the lander has range x , altitude $h = -z$, and pitch angle θ . The forces on the lander include the lander weight mg and the main engine thrust T . The moments on the lander are the torques from the reaction control jets M .

Summing the forces along the inertial axes and the moment about the body-fixed axes results in the equations of motion

$$m\ddot{x} = -T \sin \theta \quad (25a)$$

$$m\ddot{z} = mg - T \cos \theta \quad (25b)$$

$$I\ddot{\theta} = M \quad (25c)$$

To arrive at Eq. (11), solve Eq. (25b) for the thrust-to-mass ratio

$$\frac{T}{m} = \frac{g - \ddot{z}}{\cos \theta} \quad (26)$$

and substitute it and the altitude definition into Eq. (25a) as

$$\ddot{x} = -\frac{\sin \theta}{\cos \theta} (g - \ddot{z}) \quad (27a)$$

$$= -\left(\ddot{h} + g\right) \tan \theta \quad (27b)$$

Figures

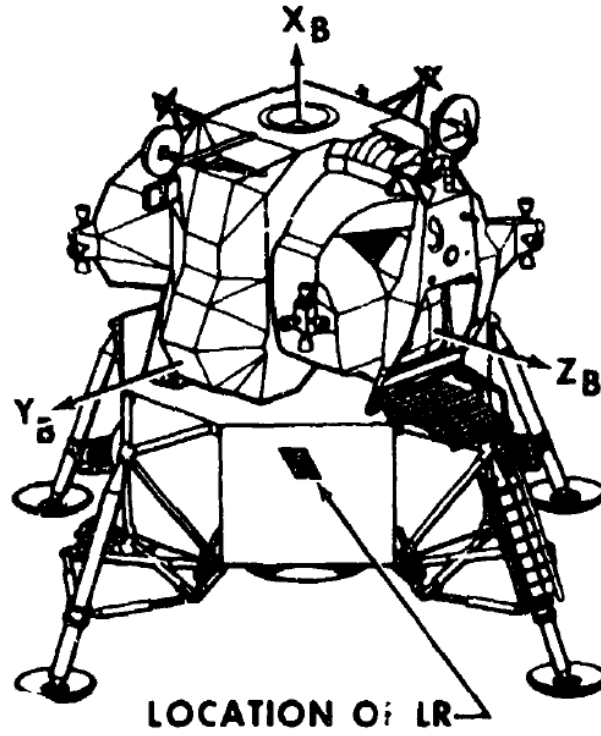


Figure 1: Lunar module and body-fixed axes (Fig. 3a in Ref. [4]).

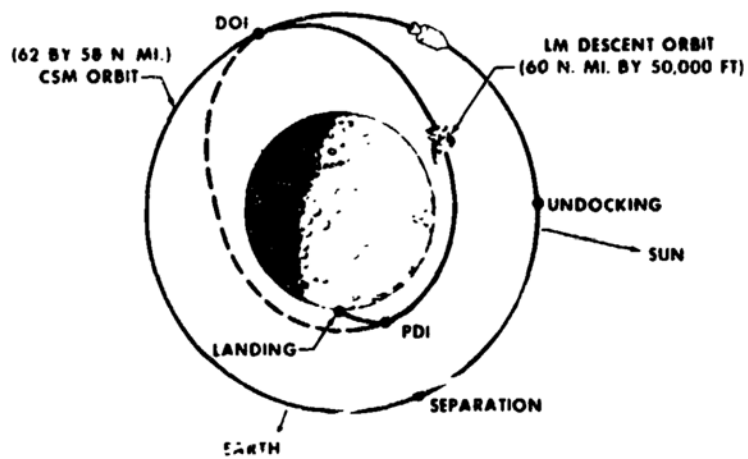
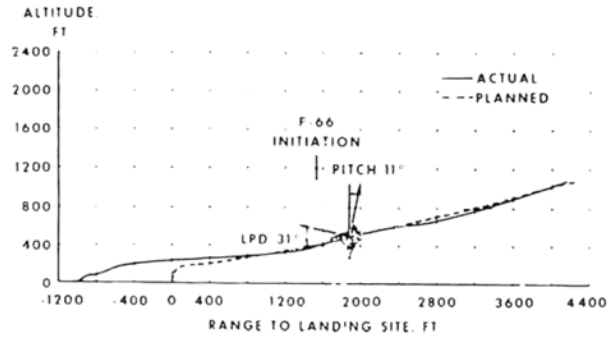
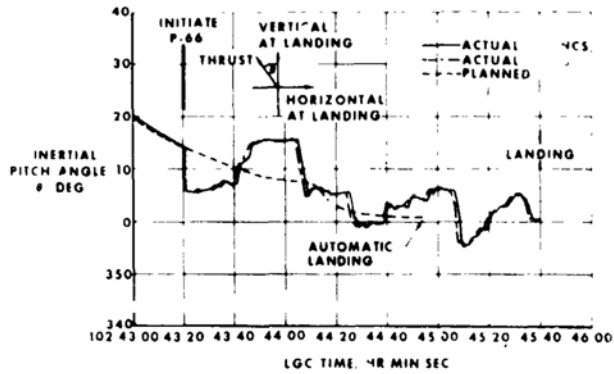


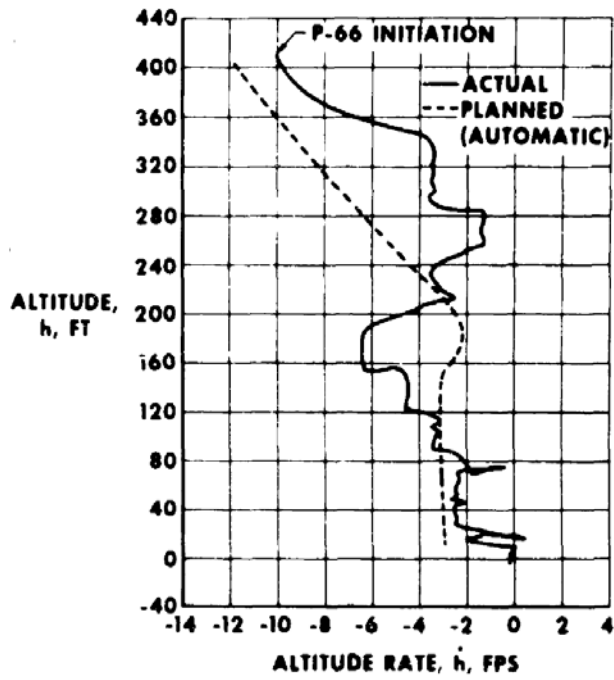
Figure 2: Lunar module descent trajectory (Fig. 1 in Ref. [4]).



(a) Range profile (Fig. 22 in Ref. [4]).



(b) Attitude profile (Fig. 24 in Ref. [4]).



(c) Altitude / altitude-rate profile (Fig. 25 in Ref. [4]).

Figure 3: Original plots of the Apollo 11 descent and landing from Ref. [4].

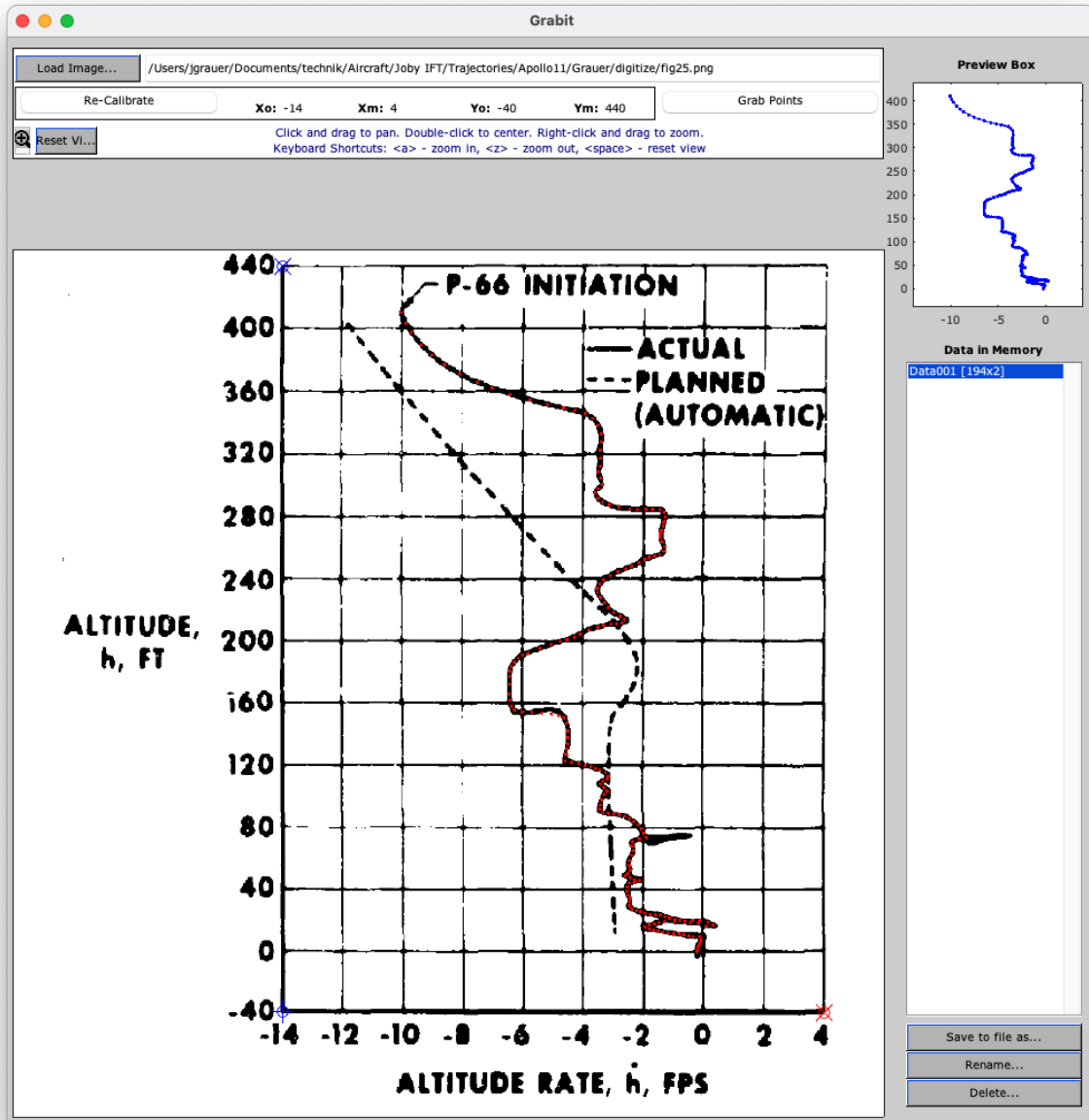


Figure 4: Digitization of altitude / altitude-rate trajectory data.

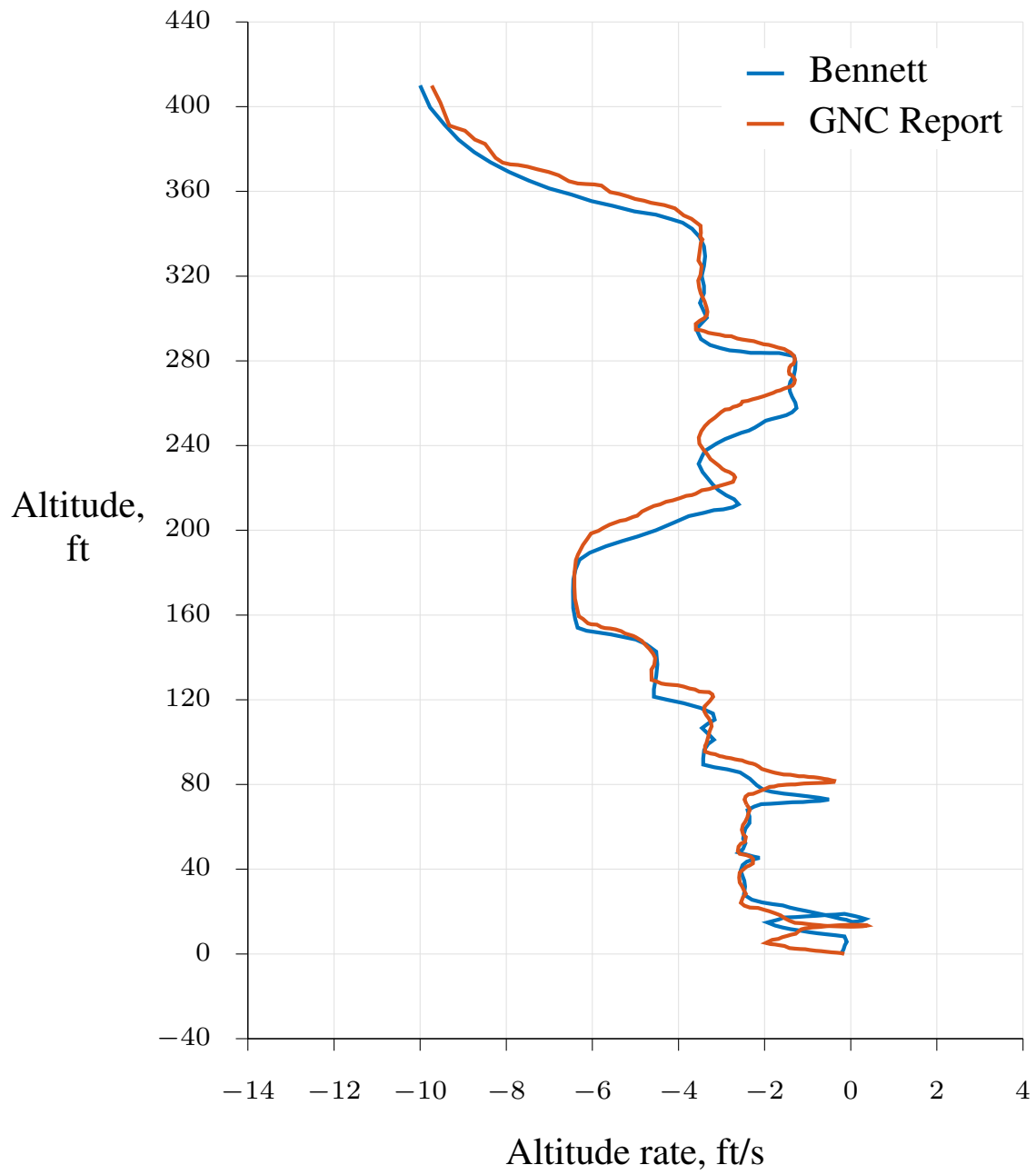


Figure 5: Comparison of altitude / altitude-rate profile from Refs. [4] and [5].

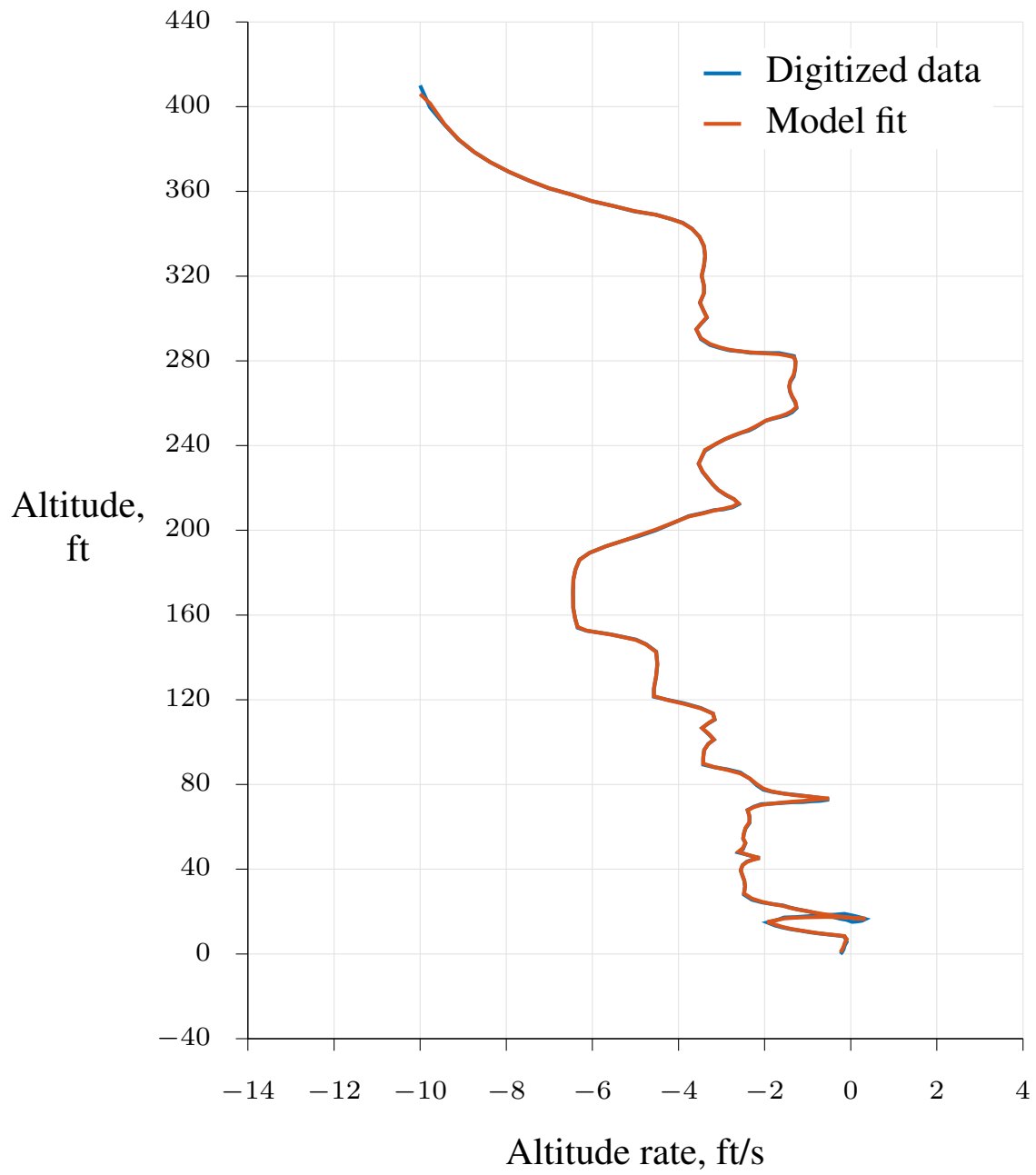


Figure 6: Fit of model output to digitized data from Bennett [4].

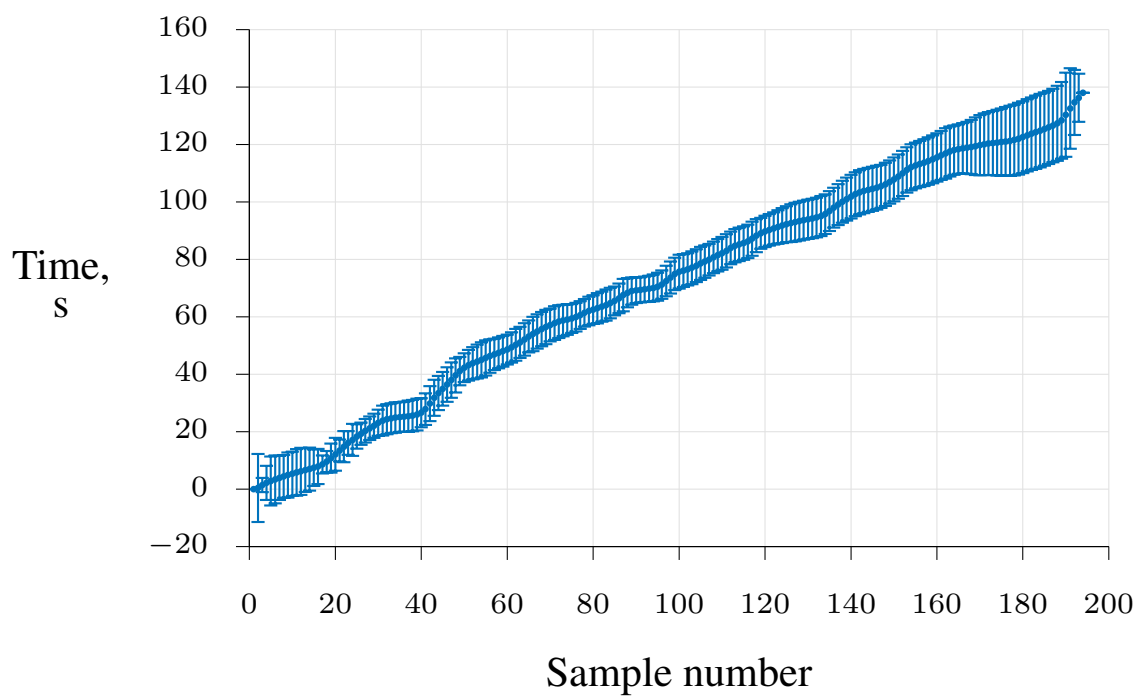


Figure 7: Estimated altitude and altitude rate time histories.

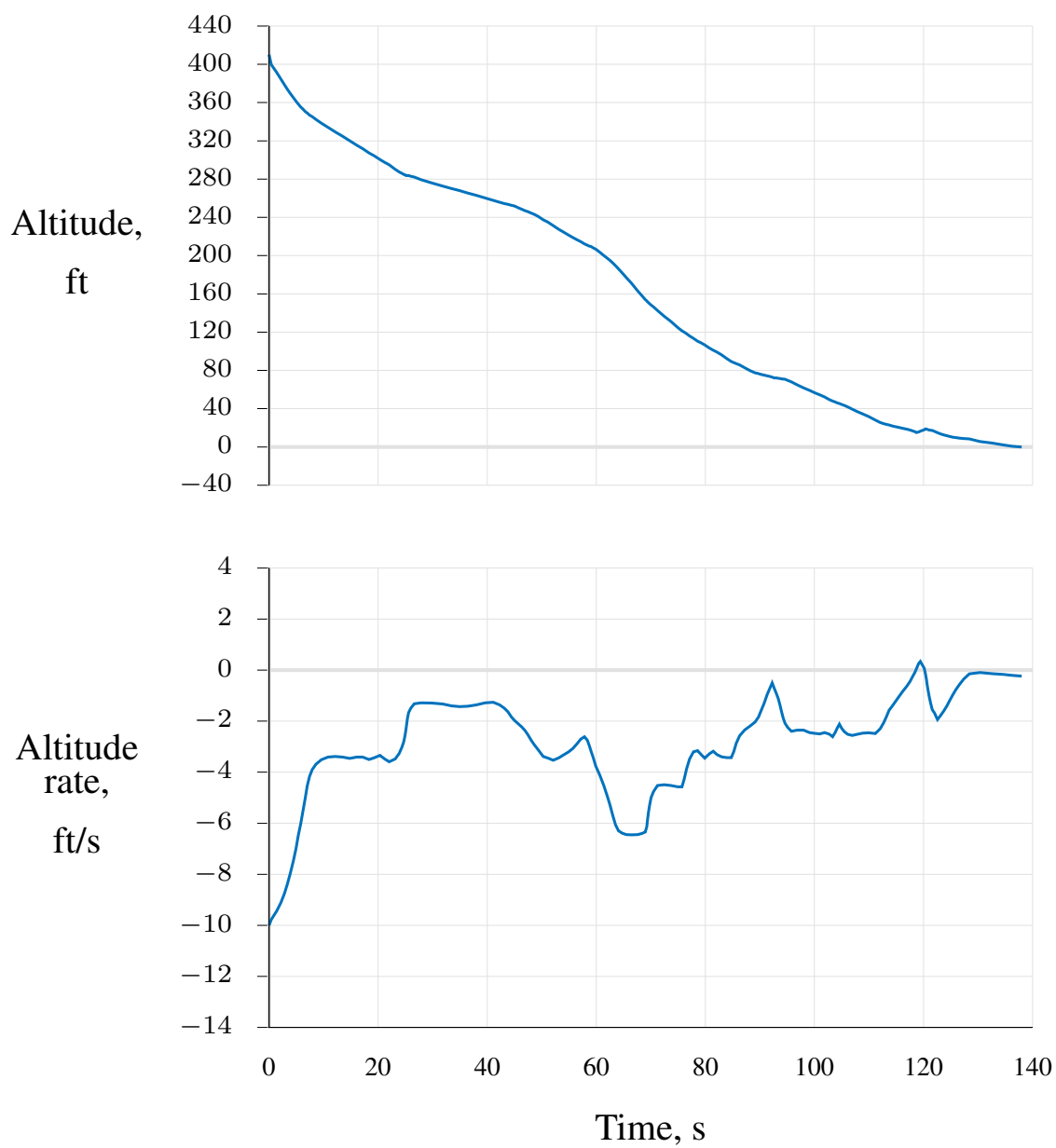


Figure 8: Estimated altitude and altitude rate time histories.

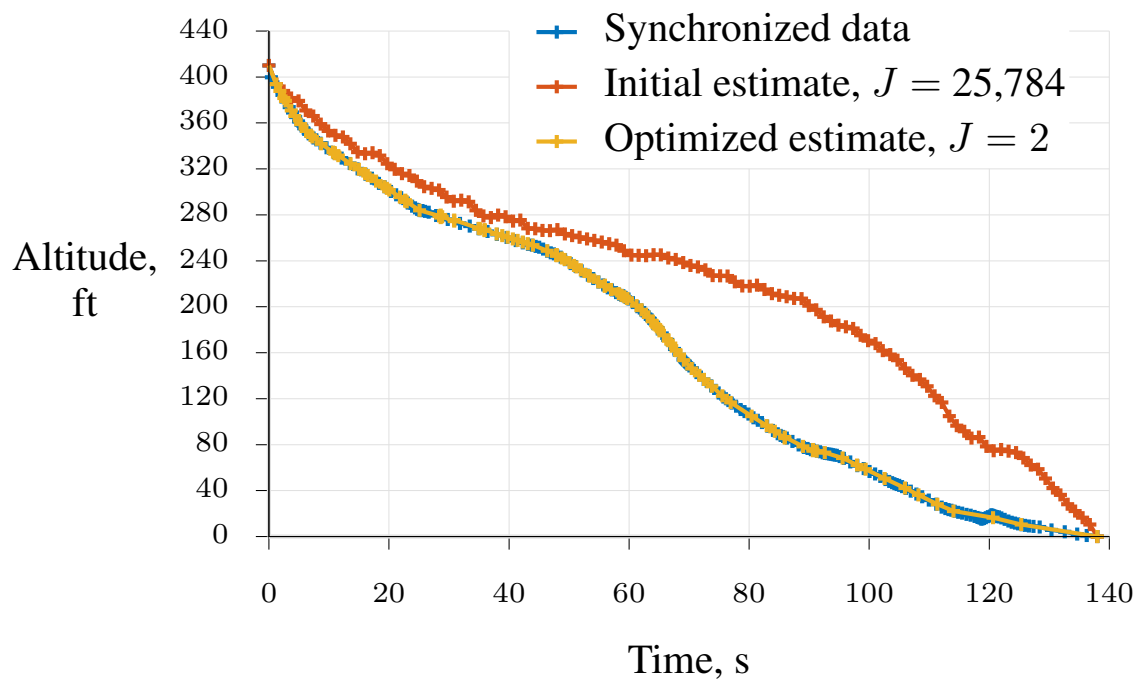


Figure 9: Estimating time samples to synchronize digitized data in Fig. 3a to Fig. 3c.

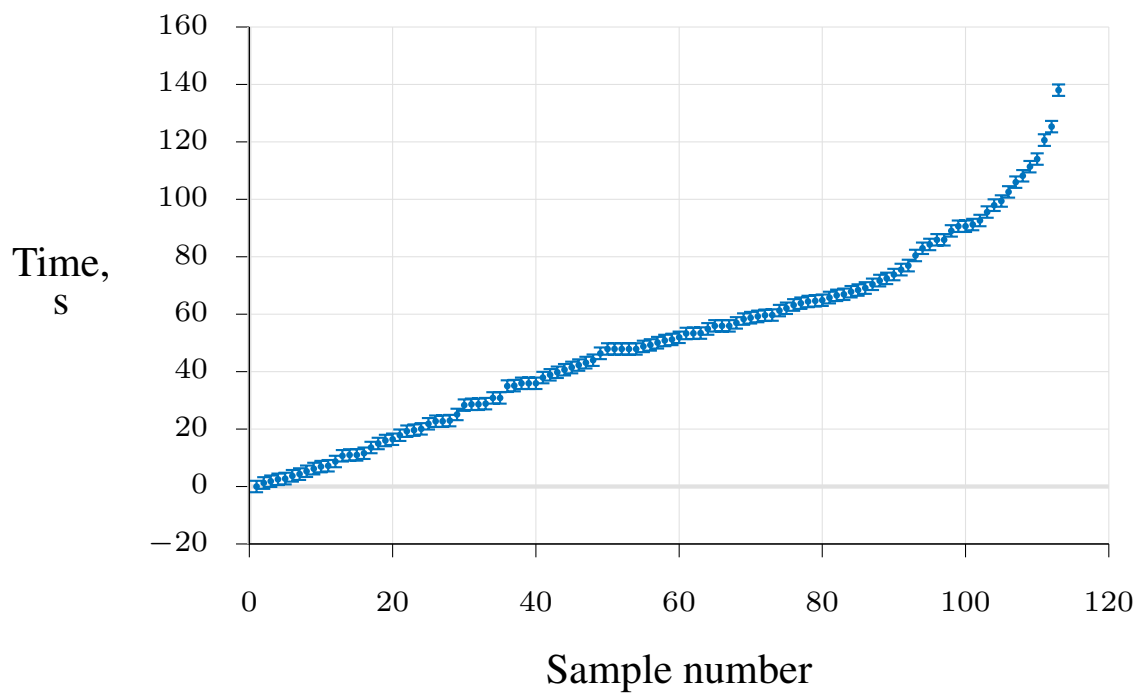


Figure 10: Estimated time samples and 95% confidence bounds to synchronize range data.

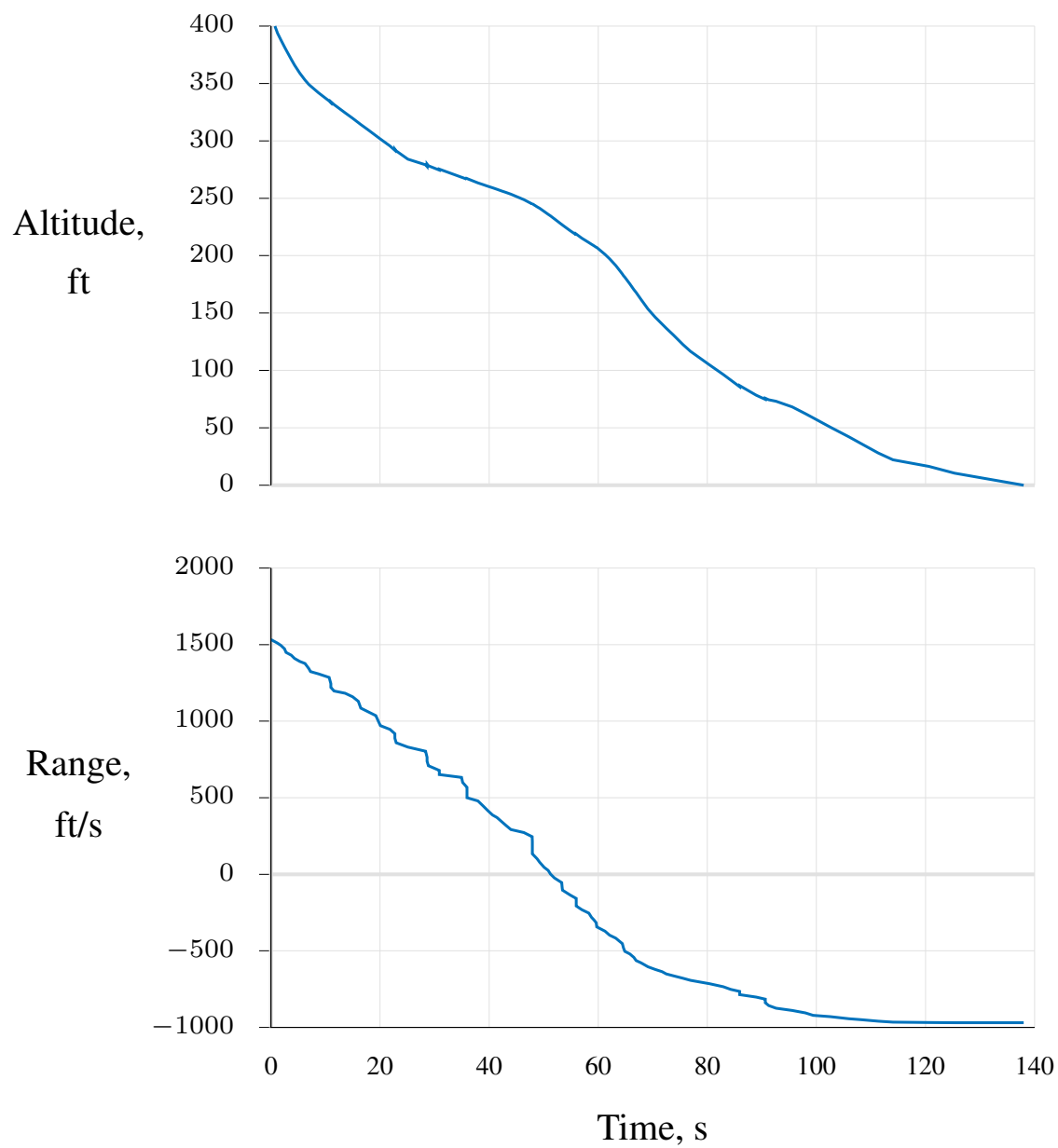


Figure 11: Synchronized altitude and range time histories from Fig. 3a.

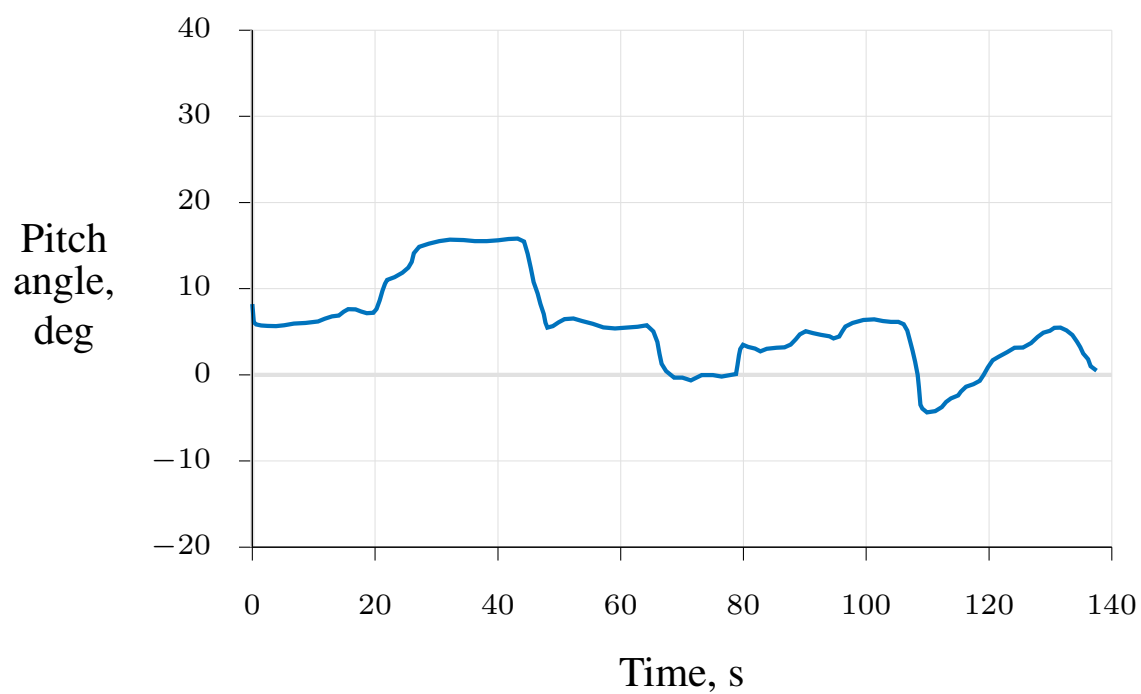


Figure 12: Pitch angle time history digitized from Fig. 3a.

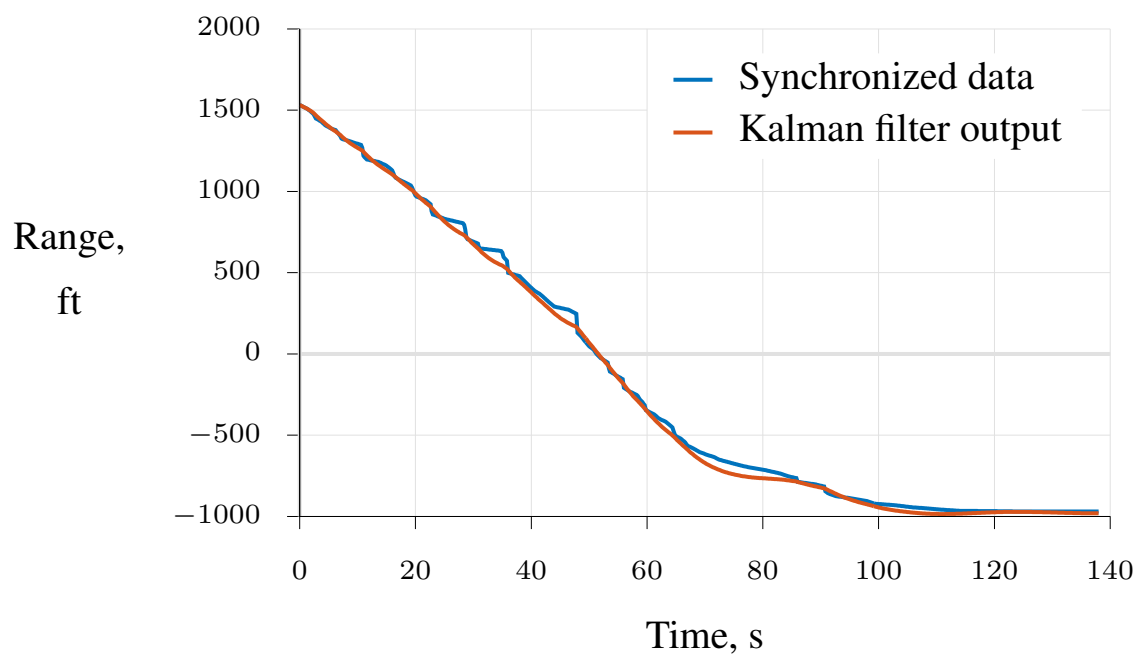


Figure 13: Range data output from a Kalman filter.

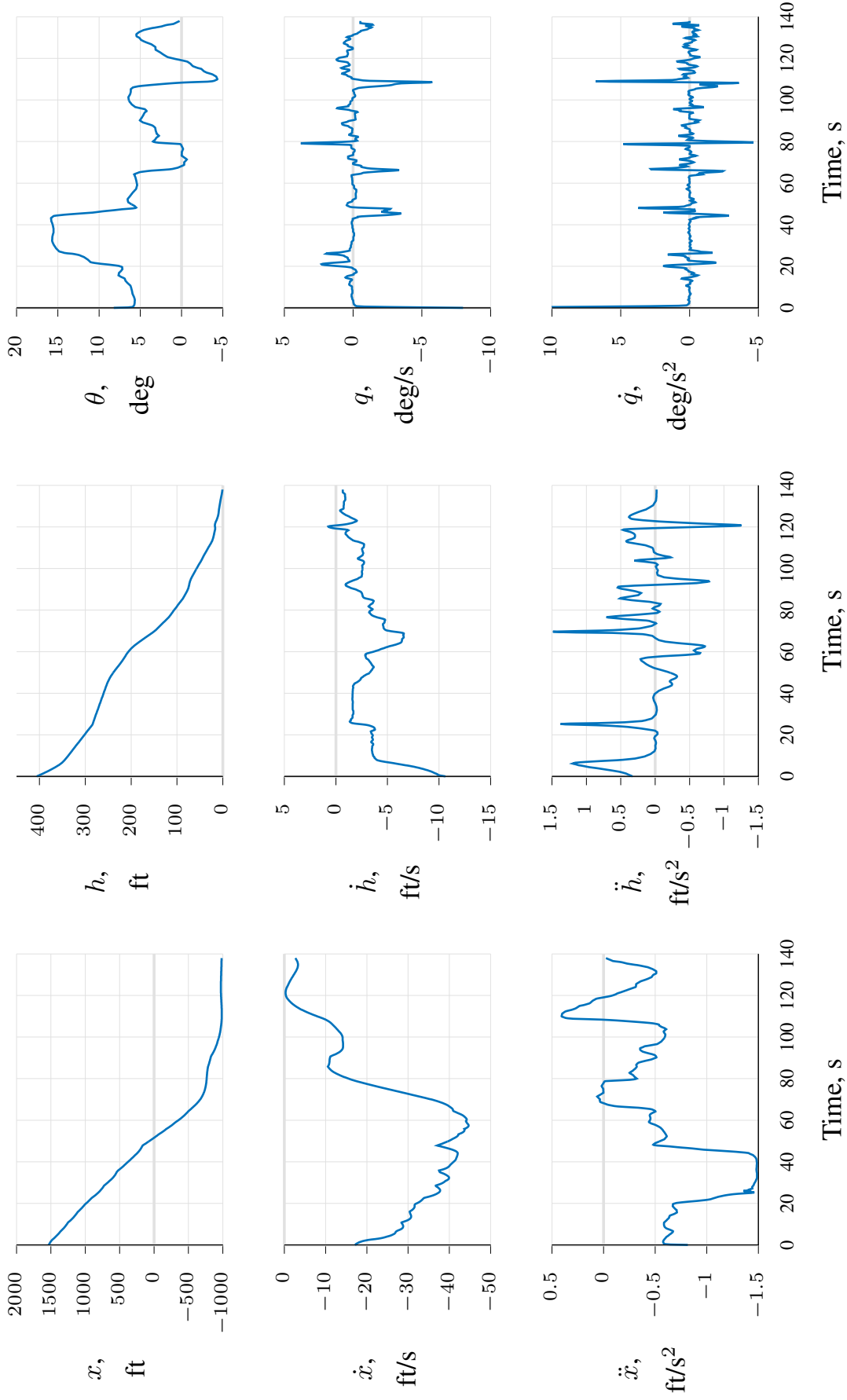


Figure 14: Total planar trajectory of the Apollo 11 moon landing final descent

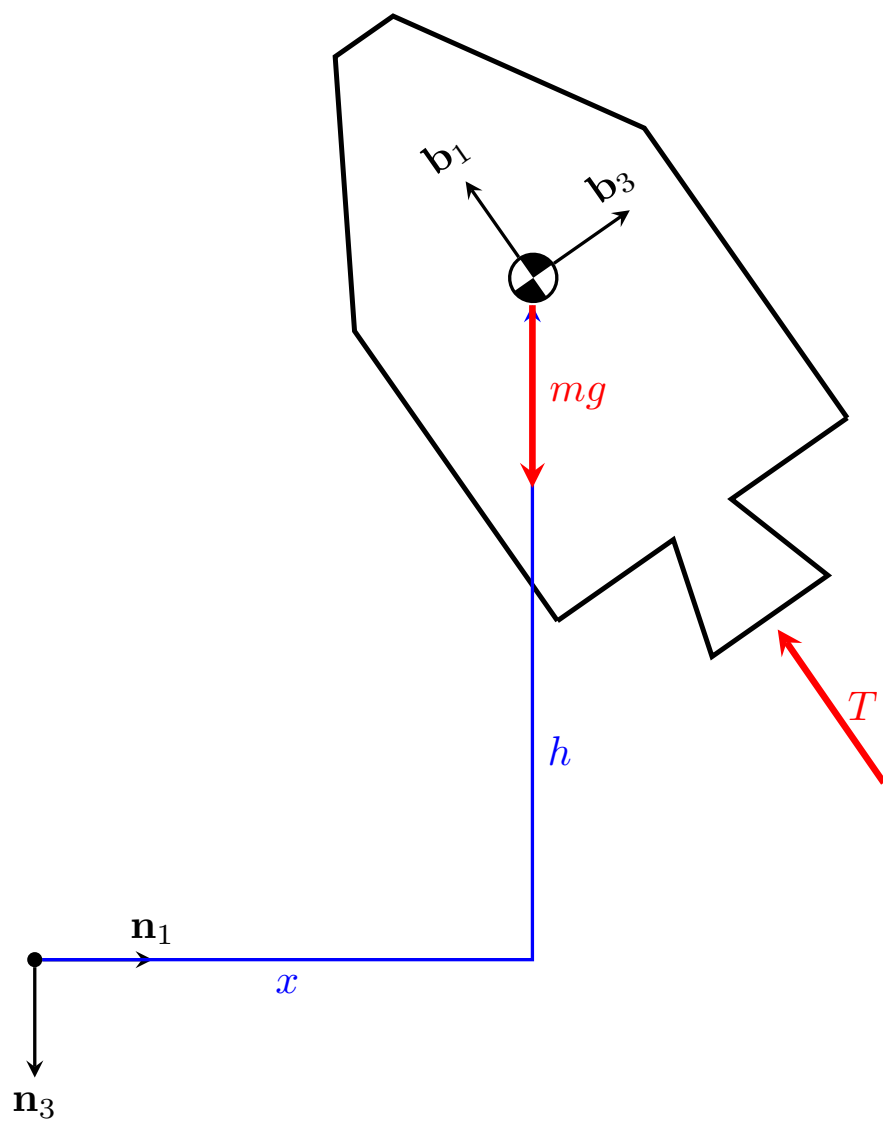


Figure 15: Free-body diagram of a simplified spacecraft model.

| REPORT DOCUMENTATION PAGE | | | | | Form Approved OMB No. 0704-0188 | |
|---|-------------|--|-------------------------------|--|---|--|
| <p>The public reporting burden for this collection of information is estimated to average 1 hour per response, including the time for reviewing instructions, searching existing data sources, gathering and maintaining the data needed, and completing and reviewing the collection of information. Send comments regarding this burden estimate or any other aspect of this collection of information, including suggestions for reducing this burden, to Department of Defense, Washington Headquarters Services, Directorate for Information Operations and Reports (0704-0188), 1215 Jefferson Davis Highway, Suite 1204, Arlington, VA 22202-4302. Respondents should be aware that notwithstanding any other provision of law, no person shall be subject to any penalty for failing to comply with a collection of information if it does not display a currently valid OMB control number.</p> <p>PLEASE DO NOT RETURN YOUR FORM TO THE ABOVE ADDRESS.</p> | | | | | | |
| 1. REPORT DATE (DD-MM-YYYY) 01-08-2022 | | 2. REPORT TYPE Technical Memorandum | | 3. DATES COVERED (From - To) | | |
| 4. TITLE AND SUBTITLE Reconstruction of the Apollo 11 Moon Landing Final Descent Trajectory | | | | 5a. CONTRACT NUMBER | | |
| | | | | 5b. GRANT NUMBER | | |
| | | | | 5c. PROGRAM ELEMENT NUMBER | | |
| 6. AUTHOR(S) Luke J. Miller, Jared A. Grauer, Jing Pei, Langley Research Center, Hampton, Virginia Stewart L. Nelson Advanced Aircraft Company, Hampton, Virginia | | | | 5d. PROJECT NUMBER | | |
| | | | | 5e. TASK NUMBER | | |
| | | | | 5f. WORK UNIT NUMBER 954879.14.23.01 | | |
| 7. PERFORMING ORGANIZATION NAME(S) AND ADDRESS(ES) NASA Langley Research Center Hampton, Virginia 23681-2199 | | | | 8. PERFORMING ORGANIZATION REPORT NUMBER | | |
| 9. SPONSORING/MONITORING AGENCY NAME(S) AND ADDRESS(ES) National Aeronautics and Space Administration Washington, DC 20546-0001 | | | | 10. SPONSOR/MONITOR'S ACRONYM(S) NASA | | |
| | | | | 11. SPONSOR/MONITOR'S REPORT NUMBER(S) NASA/TM-20220007267 | | |
| 12. DISTRIBUTION/AVAILABILITY STATEMENT Unclassified-Unlimited Subject Category 08 Availability: NASA STI Program (757) 864-9658 | | | | | | |
| 13. SUPPLEMENTARY NOTES | | | | | | |
| 14. ABSTRACT Relatively limited data on the Apollo 11 pre-planned and as-flown trajectories are available in the open literature and in the NASA archives. Furthermore, a single report appears to be the only source containing plots comparing the pre-planned and as-flown final approach and landing trajectories. The plots in that report, however, are small and difficult to read, and contain data that are insufficient for directly reconstructing the final landing trajectory. In this report, several published graphics are digitized, and then a variety of least-squares and Kalman filter estimators are applied using kinematic equations and simplified dynamic equations to reconstruct the final descent trajectory. The reconstructed trajectory is important in the crew training effort for program Artemis, which intends to send humans back to the moon, as well as other studies focusing on landing on extraterrestrial worlds. | | | | | | |
| 15. SUBJECT TERMS Frequency response, aircraft system identification, maximum likelihood estimation, output error parameter estimation, multisine inputs | | | | | | |
| 16. SECURITY CLASSIFICATION OF: | | | 17. LIMITATION OF ABSTRACT | 18. NUMBER OF PAGES | 19a. NAME OF RESPONSIBLE PERSON | |
| a. REPORT | b. ABSTRACT | c. THIS PAGE | | | STI Help Desk (email: help@sti.nasa.gov) | |
| U | U | U | UU | 32 | 19b. TELEPHONE NUMBER (Include area code) (757) 864-9658 | |